Additive Manufacturing 127 (2026) 105285

Contents lists available at ScienceDirect

Additive Manufacturing

journal homepage: www.elsevier.com/locate/addma

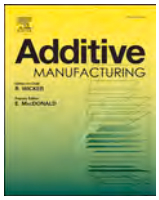

Large-scale multi-particle cold spray simulation framework for deposit morphology and deformation analysis

Xuanyu Ge, Linglong Zhou, Amir Ardeshiri Lordejani, Asghar Heydari Astaraee, Sara Bagherifard, Mario Guagliano *

Politecnico di Milano, Department of Mechanical Engineering, Milan, Italy

ARTICLE INFO

Keywords:
Cold spray additive manufacturing
Deposition process simulation
Multi-particle impact model
Extreme deformation
Cold spray shape prediction

ABSTRACT

Cold spray (CS) is a solid-state particle deposition technology extensively utilized for coating and more recently for additive manufacturing applications. While detailed numerical modeling of CS deposition offers substantial benefits for process optimization, existing methods are hindered by significant computational demands. As a result, simulations are typically confined to a small number of powder particles, which does not adequately reflect the actual deposition dynamics and therefore limits the effectiveness of simulations for deposition assessment. In this study, a high-fidelity open-source multi-particle impact framework (Free2Spray) is developed to simulate large-scale (>10,000 particles) CS deposition at a considerably convenient computational cost. The model can accurately track material changes during deposition by splitting the process into sections, each with randomly placed particles. These sections are added step by step, carrying over all data from one to the next. Python scripts are developed to automate this workflow, requiring the user to specify a few key parameters. The framework is also equipped with our recently developed high-precision material model implemented via a user-defined hardening (VUHARD) subroutine to accurately capture the realistic particle deformation. The developed framework is proven to accurately predict the shape profiles and surface roughness of experimental single-layer single-track deposits under various nozzle scanning speeds and reproduces the experimental cross-sectional particle deformation and flattening ratios. Compared with the standard Eulerian schemes, the proposed framework reduces the computational time and memory usage by 34% and 35%, respectively. These results demonstrate that the proposed framework significantly improves computational efficiency while maintaining high accuracy, enabling personal computers to simulate the CS deposition process with ten million elements and providing a reliable tool for predicting deposit morphology and particle deformation behavior. The source codes are provided (https://github.com/xuanyge/Free2Spray.git) to enable interested researchers to utilize and implement them.

1. Introduction

Cold spray (CS) constitutes a solid-state particle deposition technology in which micro-sized powders are entrained in a stream of pre-heated, high-pressure gas and accelerated to supersonic or near-supersonic velocities (300–1200 m/s) to impact a substrate and form dense deposits [1,2]. CS was traditionally applied for repair and coating fabrication [3], but it is now increasingly adopted in additive manufacturing, commonly referred to as cold spray additive manufacturing (CSAM) [4–7]. Relative to fusion-based AM methods [8], CSAM provides several distinct advantages. These include exceptionally high deposition rates, the capability to fabricate large and complex structures, broad compatibility with metals, alloys and heterogeneous materials, and the elimination of melting, which minimizes thermal residual stresses and prevents associated metallurgical degradation [9–12]. However, two main issues still restrict the application of CSAM: the relatively limited geometric accuracy of the fabricated deposits [4,13] and their suboptimal mechanical properties in as-sprayed conditions for some classes of materials [14]. It should be emphasized that addressing these issues experimentally is both challenging and costly [15]. Therefore, numerical simulations can play a crucial role in enhancing our understanding and providing reliable predictions of the CS deposit characteristics.

Currently, numerical studies on CS can be roughly divided into three

* Corresponding author.
E-mail address: mario.guagliano@polimi.it (M. Guagliano).

https://doi.org/10.1016/j.addma.2026.105285
Received 11 March 2026; Received in revised form 12 June 2026; Accepted 30 June 2026
Available online 1 July 2026

main categories: investigations of particle in-flight behavior, simulations of the particle deposition process and predictions of deposit geometry. Particle in-flight behavior is primarily simulated using computational fluid dynamics. Details like particle velocity, trajectory and temperature, as they leave the nozzle and approach the substrate, can be derived by analyzing gas-particle interactions [16–18]. Regarding deposit shape prediction, physics-based theoretical models and data-driven methods have been recently used to estimate the deposit geometry. Partial differential equations are derived from the spatial distribution of particles in the spray jet and have successfully predicted deposit profiles under multi-tracks, various spray angles, and different substrate geometries [19–21]. The data-driven methods predict deposit geometry by learning from existing datasets, enabling more accurate estimations of edge contours and complex three-dimensional surfaces [13,22]. Simulations of the particle deposition process, on the other hand, are mainly based on the Lagrangian and Eulerian schemes of the finite element method (FEM), meshless methods such as smoothed particle hydrodynamics (SPH) and molecular dynamics (MD) [23]. The Lagrangian scheme can accurately track the deformation of individual particles [24]. However, it suffers from convergence issues due to excessive element distortion in high-velocity impacts and multi-particle scenarios [25,26]. In contrast, the Eulerian scheme can accommodate large deformations and continuous material flow without mesh distortion, making it well-suited for multi-particle simulations [27–29]. The pioneering coupled Eulerian-Lagrangian (CEL) framework developed by Li et al. [30–33] has been demonstrated to accurately capture particle deformation behavior and predict the critical velocity. SPH effectively handles free surfaces and large deformations, yet its accuracy strongly depends on the particle resolution and ensuring numerical stability when subjected to tensile stress remains difficult [34,35]. MD can capture microscopic particle interactions and nanoscale effects, providing detailed insights into deposition mechanisms; however, its high computational cost restricts its direct applicability to macroscopic analysis [36,37].

While these simulation approaches primarily support process optimization and deposit characterization from different perspectives, they are fundamentally constrained by their application to systems that are significantly smaller than those encountered in practical CS deposition. As a result, the predictive capacity of current models remains limited. Thus, the development of a modeling framework capable of bridging this scale gap would represent a substantial advancement, offering more comprehensive and reliable insights for both process optimization and deposit physical and mechanical characterization. High-fidelity simulation approaches have been widely applied in other AM techniques [38–41]. For CS simulations, achieving real-scale modeling appears to be challenging. Most multi-particle CS simulations rely on the Eulerian scheme, in which particles must be discretized as material volume fractions (VFs) within the Eulerian mesh. This approach is inherently inefficient because it requires a very large number of elements. Besides, the accuracy of the Eulerian scheme is restricted by mesh resolution, as a coarse mesh is inefficient to adequately discretize particles [42,43]. Moreover, when the number of particles increases, the Eulerian domain must be enlarged accordingly, further increasing the total number of elements. As a result, the maximum number of particles modeled in previous studies with the Eulerian scheme has been limited to approximately 500 [28]. In a recent study, Zhang et al. developed a customized SPH framework to simulate a real-scale CS process involving up to 200,000 particles [44]. Using this large-scale SPH model, they successfully predicted the cross-sectional profile of the AISI 316 L deposit and further predicted the porosity of the deposits by adopting a refined SPH resolution. The efficiency of the developed SPH framework was achieved through 24-core CPU parallelization, enabling a multi-particle deposition simulation involving up to 14,527,275 degrees of freedom within 30 h [44]. Despite recent advancements in SPH methods, FEM-based approaches remain highly attractive for CS simulations due to their wide engineering application, mature constitutive models, and superior computational efficiency. Furthermore, their inherent compatibility with downstream structural mechanics analyses facilitates the direct mapping of Lagrangian or Eulerian simulation results into other FEM models for subsequent mechanical property evaluation [45–48]. Therefore, the Eulerian scheme appears to be a more suitable choice for extended CS multi-particle simulation and analysis; however, it necessitates fine discretization of powder particles, which significantly reduces computational efficiency [33]. Therefore, enhancements to the standard Eulerian scheme are essential to facilitate large-scale simulations.

From another point of view, in CS simulations, the material constitutive model is one of the most important factors determining the accuracy of the results. Johnson–Cook (JC) model [49] remains the most widely adopted constitutive model, as it incorporates the effects of strain hardening, strain rate hardening, and thermal softening on flow stress. Nevertheless, some studies have shown that the JC model tends to significantly exaggerate particle deformation in CS applications [50–52]. This limitation stems from the fact that JC was originally calibrated for strain-rate regimes ($<10^4\ s^{-1}$) that are significantly lower than those typically encountered in CS ($\sim10^7–10^9\ s^{-1}$) [50]. To overcome this deficiency, modified JC [52] and other [53,54] constitutive models have been introduced to better capture the extreme particle deformation in CS. Recently, we developed a new material model for CS simulations (hereafter referred to as the Ge model) and validated its accuracy by simulating the impact behavior of copper (Cu) particles deposited over a wide range of velocities [55]. However, currently the accuracy of our model has been evaluated only for predicting single-particle impact deformation, and further investigations are required to assess its reliability in simulating material behavior at size-realistic CS impact scenarios.

To address the abovementioned challenges, herein, we propose an original open-source multi-particle impact framework to simulate the large-scale CS deposition process. The framework is implemented using an upgraded Eulerian scheme in Abaqus, which adopts a recurring simulation strategy to substantially improve computational efficiency. In this framework, several particle batches with random spatial distribution are generated, and the corresponding VFs are calculated using a pre-processing Python script. Recurring simulations are then conducted by applying the execution script. Moreover, the framework integrates our recently developed high-precision material model to describe the particle deformation behavior. Compared with the standard Eulerian scheme, the proposed framework offers a significant reduction in computational cost, both in terms of runtime and memory consumption, while maintaining high predictive accuracy. Single-track and multi-track deposition experiments at different scanning speeds were conducted to validate the results of the proposed framework. The capability of the framework was demonstrated by accurately reproducing the overall profiles, local surface roughness and particle flattening ratios of various CS deposits. The results indicate that the proposed computational framework provides a high-fidelity and efficient tool for both large-scale morphology prediction and particle-scale analysis in CS deposition processes.

This paper is structured as follows. Section 2 details the experimental setup for single- and multi-track deposition. Section 3 introduces the proposed framework and the corresponding material model. Section 4 assesses the computational efficiency of the proposed framework, and Section 5 validates the model through comparisons between simulation results and experimental data. Finally, the main conclusions are summarized in Section 6.

2. Experimental set-up

In this study, pure Cu powder and pure Cu substrates were chosen as the target materials. Previous work demonstrated that properly designed CS processing can improve the ductility of Cu deposits without compromising strength, providing an important insight into the CSAM

[56]. A commercial spherical Cu powder (Safina, CZ) with a purity of 99.5% and a particle volume distribution of D10 = 19 μm, D50 = 30 μm, and D 90 = 52 μm was used as the powder feedstock, with particle diameter ranging from 10 to 85 μm. Cu substrates of 62 × 20 × 3 mm3 were cut and polished before deposition. An Impact 6/11 CS gun equipped with a tungsten carbide de Laval nozzle (Out1, Impact Innovations, DE) was used for the CS deposition experiments, as shown in Fig. 1(a). The nozzle geometry included a throat diameter of 1.35 mm, an exit diameter of 3.2 mm, a converging section length of 50 mm, and a prechamber diameter of 12 mm. For all experiments, N_2 was used as the carrier gas, and gas temperature and pressure were set to 750 ℃ and 40 bar, respectively. Powder feed rate and stand-off distance were fixed at 42.2 g/min and 30 mm, respectively. For different samples, only the scan strategy and scanning speed were varied, as listed in Table 1. First, single-layer single-track CS depositions were performed with three different scanning speeds to obtain the profile of the single-track deposits with varying thicknesses. Subsequently, a multi-layer multi-track CS deposition was conducted to get a relatively thick deposit, which was used to examine the particles' flattening ratio within the deposit.

For realistic deposition simulations, HiWatch HR2 (Oseir Ltd., FI) was used to measure particle velocities, diameters, and positions in the gas flow, as shown in Fig. 1(b). The HiWatch system determines particle size using laser scattering imaging as particles pass through an illuminated laser sheet. Particle velocity is calculated using a time-of-flight method by tracking their displacement between two closely spaced exposures. Particle position is recorded within the imaging plane, based on the detected location of individual particles [44].

After deposition, the single-layer single-track samples were first scanned by Mech-Eye UHP−140-GL 3D camera (Mech Mind Ltd., CN) to acquire the deposits' geometry. Then, the samples were cut perpendicular to the scanning direction and englobed into resin pucks for profile and metallographic analysis.

The englobed samples were subsequently prepared through grinding, polishing and ultrasonic cleaning until the deposit's cross-section was scratch-free and ready for microscopic observation. For each single-layer single-track sample, 20 images of the cross-section were captured and merged to form a panoramic view. The cross-section of the multi-layer multi-track sample was chemically etched for 30 s using a saturated $Na_2S_2O_3$ + 40 g $K_2S_2O_5$ solution [57] to reveal the particle-particle interfaces prior to the microscopic observation. All samples were examined using an Eclipse LV150NL light optical microscope (OM)(Nikon, JP).

Table 1
Scan strategy and scanning speed for different samples.

Sample No.	Scan type	Scanning speed V_s (mm/s)
1	Single-layer single-track	160
2	Single-layer single-track	120
3	Single-layer single-track	80
4	Multi-layer multi-track	80

3. Multi-particle computational framework

An Eulerian-scheme multi-particle impact framework is developed to overcome the limitations of standard Eulerian CS simulations. This framework, termed "Free2Spray", reflects its goal of enabling a simpler and more flexible approach for simulating the CS deposition process, particularly for large-scale multi-particle impact problems on ordinary personal computers. Although continuous analysis in Abaqus can be achieved using *Restart or *Initial state functions in the commonly used Lagrangian scheme, such approaches are primarily intended to continue an existing analysis while preserving the original computational domain and model configuration. Moreover, due to the severe deformation involved in particle impact, large-scale multi-particle Lagrangian simulations commonly suffer from mesh distortion and convergence difficulties, making the Eulerian scheme more suitable for CS deposition problems. However, conventional restart approaches cannot be directly applied to Eulerian simulations, since material placement is governed by the VF field, which cannot be automatically reconstructed through standard restart procedures. To overcome these limitations, Free2Spray is developed as an automated recurring simulation framework capable of maintaining physically continuous deposition through sequential simulation cycles. The framework is implemented within the commercial FEM software Abaqus and is naturally divided into two components: "Pre-processing" and "Simulation execution". In the pre-processing stage, the framework automatically calculates the VF field, extracts corresponding node sets from generated.inp files, and assigns initial velocity and temperature conditions to particle and substrate regions, thereby substantially reducing the labor-intensive setup typically required in Eulerian analyses. During simulation execution, key state variables, including VF, PEEQ, temperature, velocity, and stress, are transferred between successive cycles, while newly generated particle batches with randomized spatial arrangements replace particles leaving the deposition region, enabling continuous deposition and efficient computation without enlarging the Eulerian domain. In addition, the recently developed Ge model [55] is incorporated into the framework to enhance simulation accuracy. The components of the framework are

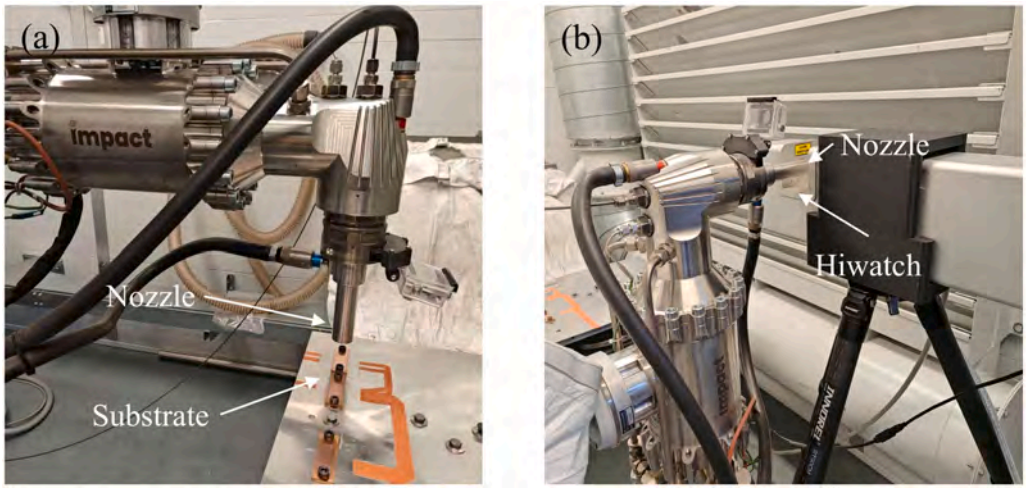

Fig. 1. (a) Cu deposition on Cu substrate using the high-pressure CS system; (b) Measurement of particle velocities, diameters and positions in the gas flow using the HiWatch system.

discussed separately in the following sections.

3.1. Free2Spray: pre-processing

To perform Eulerian analysis in Abaqus, it is essential to encapsulate the simulated entities within the Eulerian domain to enable the calculation of their VF [33]. For multi-particle CS simulations, a uniform mesh size is typically used throughout the entire Eulerian domain to ensure sufficient accuracy [27]. However, traditional multi-particle Eulerian simulations can be inefficient, as much of the mesh becomes inactive once particles deposit. To address this, a new approach is proposed, splitting the domain into three layers: flying particles (top), substrate (bottom), and impact region (middle), as shown in Fig. 2(a) and (b). Simulations proceed in cycles, once all particles have exited the top layer, the results (e.g. stress, strain, temperature and VF) are extracted and a new set of particles is introduced to substitute them, as shown in Fig. 2(c). A Python script automates initialization, particle distributions, material definitions, field assignments, and iterative file generation, handling the challenges of randomness and node assignment, thus maintaining simulation accuracy and efficiency. This method enables continuous particle deposition using the Eulerian scheme while reducing the number of required elements, resulting in significant memory and computational savings.

The pre-processing workflow consists of three steps: reading particle distribution and creating instances for particles, substrate, and domain; initializing material properties, analysis steps, and boundary conditions; and finally computing VF while assigning velocities and temperatures to particles and substrate nodes. Although the pre-processing workflow is not inherently complex, its implementation involves two major challenges. To begin with, the way particles are distributed in the CS powder flow is random to replicate the real spraying condition. If the created particle batches are used repeatedly for deposition, the results will be much less accurate compared to results from the standard Eulerian method. Secondly, although using a script to compute the VF is supported in Abaqus, the node sets (required for assigning temperature and velocity) associated with these VF can only be created through the Abaqus CAE interface, making the process highly inconvenient.

To resolve these issues, the workflow is updated to include a loop in the Python script that generates multiple particle VF and the corresponding node sets. In each iteration, a particle batch is selected, pre-processing is performed, and the resulting VF, node sets, and nodal velocity field are saved as.inp files for subsequent use. In the second round, the earlier particle group and VF are removed, and a new batch of particles is used to create the corresponding instances, compute their VF, extract the relevant node sets, and determine the velocity field. This process is repeated for each particle batch until all batches are handled. Once the last batch is processed, the substrate VF is calculated, and the substrate set is assembled. Finally, an.inp file is generated that assigns temperature fields to both the particles and the substrate.

In the developed script, the user must define the length l_e, width W_e and height H_e of the Eulerian domain, as well as the substrate height H_s and the particle layer height H_p, as shown in Fig. 2. In addition, the mesh size, the number of particle batches, material properties and the analysis step must be specified. These variables can be easily modified based on the source code provided. To help readers better understand the developed script, the relevant flowchart is presented in Fig. 3.

3.2. Free2Spray: simulation execution

After the pre-processing stage, the simulation is executed to simulate the continuous particle depositions. To maintain physically continuous deposition in the Eulerian scheme, the simulation execution stage is designed as a recurring process in which the results of the previous cycle are transferred to the subsequent analysis. The Python script developed to implement the simulation execution starts by scanning the working directory to collect groups of.inp files containing particle VF, node sets and velocity fields. For each cycle, the script randomly selects one group and modifies the original.inp file and inserts the *Included files for the particle VF, node sets and velocities obtained from pre-processing. In the first iteration, a new analysis job is created and submitted using the modified.inp file and a customized user subroutine. When all particles flow out of the initial particle region, the simulation terminates, and the stress, PEEQ, temperature and velocities are extracted and written into individual.inp files. The.odb file from each cycle is renamed to prevent overwriting. In the next iteration, the.inp files extracted from the previous step are considered to start the simulation. This procedure is repeated until the final iteration. In the last iteration, the step time in the.inp file must be modified to ensure complete particle deposition before the final simulation is performed.

A flowchart of the developed script is presented in Fig. 4. It should be noted that the number of iterations in the execution stage can be set higher than the number of batches generated in the pre-processing stage (e.g., five particle batches with ten simulation iterations) to save computational time.

3.3. Material model

Recently, we developed a new material model (Ge model) [55] and

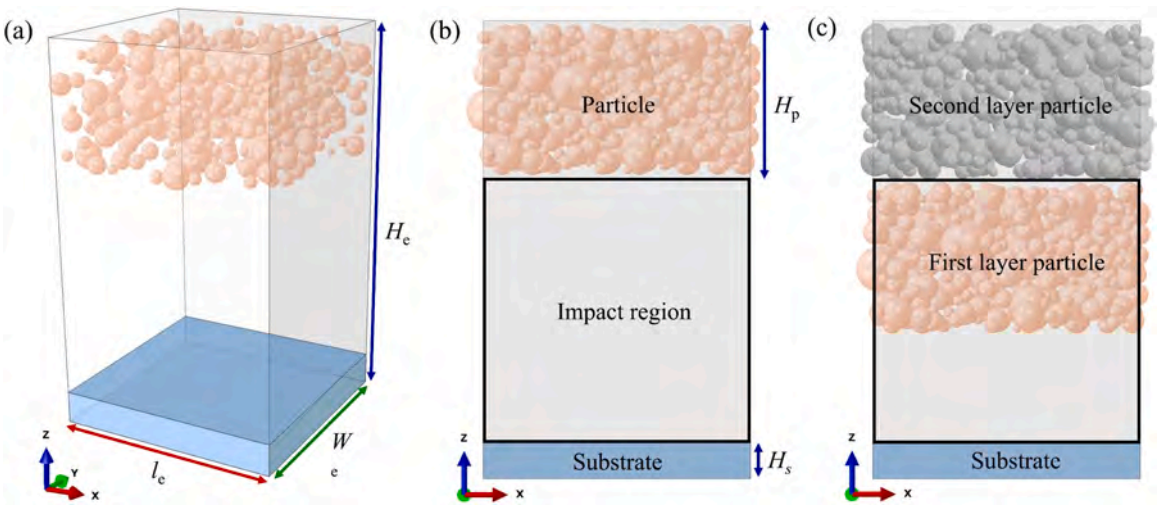

Fig. 2. The size and partitioning of the Eulerian domain used in the proposed approach: (a) 3D view and (b) x–z plane view. (c) The relative position between the second batch of placed particles and the first batch after the first particles leave the top layer.

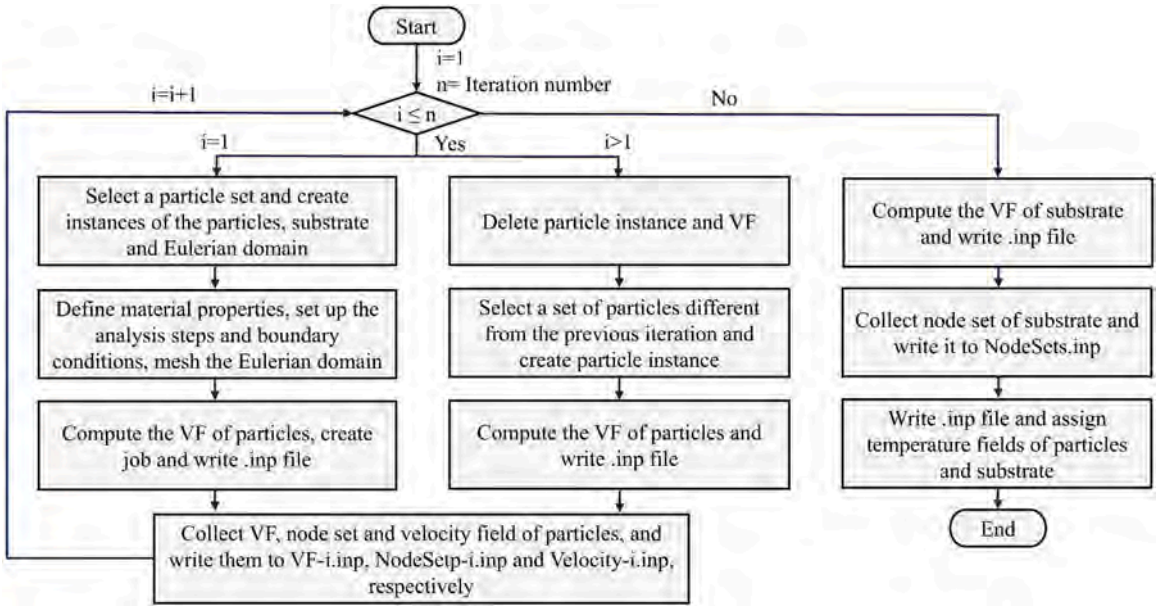

Fig. 3. The flowchart of the developed script for Free2Spray pre-processing.

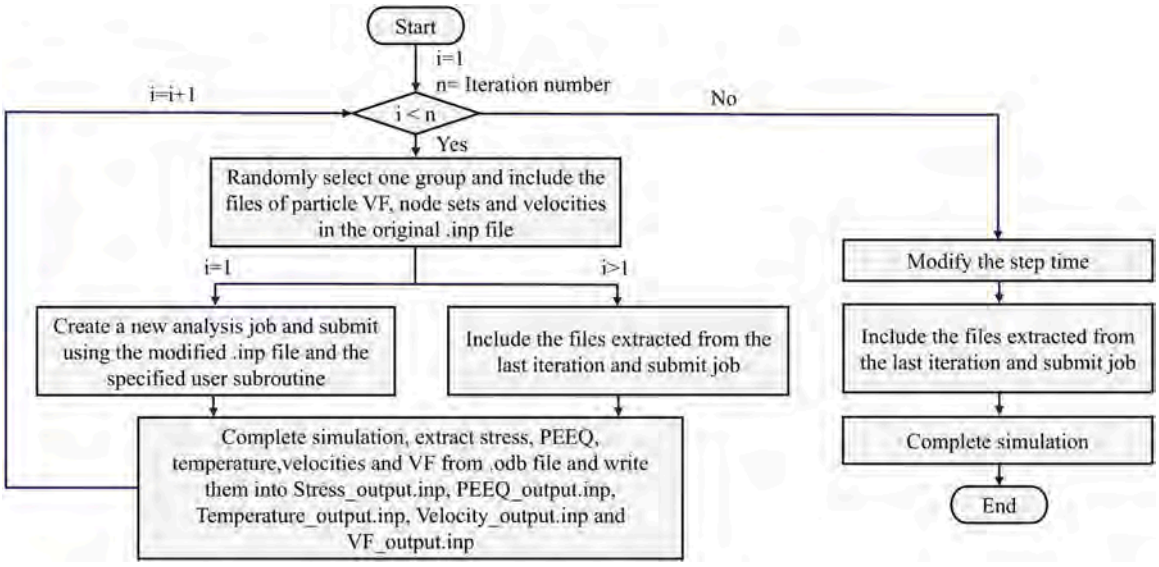

Fig. 4. The flowchart of the developed script for Free2Spray simulation execution.

adopted it in the present study to more accurately predict the material deformation behavior under extreme thermomechanical loading conditions. The detailed formulation derivation, calibration procedure, and quantitative validation of the model are provided in the previous study [55]. Specifically, the model accounts for the effects of equivalent plastic strain (PEEQ), PEEQ rate, and temperature on the flow stress, and is expressed as:

$$\sigma_y = \left[\underbrace{\left(\sigma_{y0} + A{\varepsilon_p}^n\right)}_{\text{Strainhardening}} + \underbrace{\left(\alpha{\varepsilon_p}^n + \beta\right)\ln\left(\frac{\dot{\varepsilon}_p}{\dot{\varepsilon}_s}\right)}_{\text{Normalstrainrate}} + \underbrace{B\ln\left(\frac{\dot{\varepsilon}_p}{\dot{\varepsilon}_u}\right)}_{\text{Highstrainrate}} \right] \left(\underbrace{\frac{1+e^{(T_r-T_{ref})\eta}}{1+e^{(T-T_{ref})\eta}}}_{\text{Thermalsoftening}} \right) \tag{1}$$

where σ_y represents the flow stress, which depends on the PEEQ ε_p, PEEQ rate $\dot{\varepsilon}_p$ and temperature T. Parameters $\dot{\varepsilon}_s$ and $\dot{\varepsilon}_u$ are the reference PEEQ rates, corresponding to the ranges of normal and high strain rate hardening, respectively. T_r is the room temperature, while T_{ref} is the reference temperature at which the flow stress decreases most rapidly. η is a fitting parameter that governs the rate of decrease of the flow stress.

Ge model can be implemented in Abaqus in its simplest way using a user-defined plasticity (VUHARD) subroutine. In VUHARD, it is only necessary to define the flow stress formulation, as well as the derivatives of the flow stress with respect to ε_p, $\dot{\varepsilon}_p$ and T, which can be expressed as:

$$\frac{\partial\sigma_y}{\partial\varepsilon_p} = \left[nA{\varepsilon_p}^{n-1} + \alpha n{\varepsilon_p}^{n-1}\ln\left(\frac{\dot{\varepsilon}_p}{\dot{\varepsilon}_s}\right)\right]\left(\frac{1+e^{(T_r-T_{ref})\eta}}{1+e^{(T-T_{ref})\eta}}\right) \tag{2}$$

$$\frac{\partial\sigma_y}{\partial\dot{\varepsilon}_p} = \left(\frac{\alpha{\varepsilon_p}^n + \beta + B}{\dot{\varepsilon}_p}\right)\left(\frac{1+e^{(T_r-T_{ref})\eta}}{1+e^{(T-T_{ref})\eta}}\right) \tag{3}$$

$$\frac{\partial \sigma_y}{\partial T} = \left[\left(\sigma_{y0} + A\varepsilon_p{}^n\right) + \left(\alpha \varepsilon_p{}^n + \beta\right) \ln\left(\frac{\dot{\varepsilon}_p}{\dot{\varepsilon}_s}\right) + B \ln\left(\frac{\dot{\varepsilon}_p}{\dot{\varepsilon}_u}\right) \right] \left\{ \frac{-(1 + e^{(T_r - T_{ref})\eta})\eta e^{(T - T_{ref})\eta}}{[1 + e^{(T - T_{ref})\eta}]^2} \right\} \quad (4)$$

The material parameters for the Cu particles and substrate used in this study have been previously calibrated for the Ge model [55], as listed in Table 2.

4. Free2Spray framework fidelity and efficiency

To verify the accuracy and efficiency of the proposed framework, the relevant results were compared to the standard Eulerian scheme. The model was created to simulate the deposition process of 5000 particles. First, a MATLAB script was developed to create particles in space, making sure that the gap between each particle and its neighbors was more than 1.5 times their combined radii to avoid any overlap [26]. In the proposed framework, five sets of particles' (containing 500 particles each) VF were calculated before the simulation started, and ten random runs were carried out during the simulation. The model and particle distribution for the proposed framework are shown in Fig. 2; whereas, for the standard Eulerian scheme, the VF of all 5000 particles was computed in the same model with an overview of the model and particle distribution shown in Fig. 5. For both the proposed framework and the standard Eulerian scheme, particle sizes were generated following a Rosin–Rammler distribution [26] that reproduces the experimental volume distribution presented in Section 2.

Since materials with pronounced thermal softening (e.g., Cu) may flow out of the Eulerian domain during deposition, symmetric boundary conditions were applied in the x and y directions to suppress material outflow. Although this approach may introduce complex particle-boundary interaction, its effect on the central deposition zone was considered negligible, ensuring that the overall simulated deposition behavior remains physically representative. The proposed framework used the following settings: $l_e = 0.35$ mm, $W_e = 0.35$ mm, $H_e = 0.6$ mm, $H_s = 0.05$ mm, and $H_p = 0.203$ mm, where the domain height was determined by the target deposit height and the particle batch region height in each recurring cycle. For the standard Eulerian scheme, the corresponding values were $l_e = 0.35$ mm, $W_e = 0.35$ mm, $H_e = 2.01$ mm, $H_s = 0.05$ mm, and $H_p = 2.003$ mm, with the domain height selected as the minimum size required to accommodate the prescribed particle number. The selected domain height mainly affects the number of deposited particles, with limited influence on deposition behavior. The Eulerian domain and substrate were designed to match the area exposed to the particle batch. This configuration was adopted to balance computational efficiency and simulation fidelity, focusing mostly on the deposited material rather than the substrate and the stress wave propagation that are expected to be affected by the model size. Therefore, the selected domain size was considered sufficient for evaluating the deposition behavior.

For both approaches, the mesh size was set to 3 μm, resulting in a total of 2737,800 and 9579,712 Eulerian 8-node thermally coupled reduced-integration solid elements (EC3D8RT) for the proposed framework and the standard Eulerian scheme, respectively. Although particle velocity is generally size dependent, the results in Fig. 8 showed limited sensitivity to particle diameter under the present spraying conditions. Therefore, a uniform particle velocity of 615 m/s and an initial particle temperature of 450 ℃ were adopted for pre-processing convenience. The substrate temperature was set at 25 ℃.

Table 2
Material parameters of Cu and Ge model [55].

Young's modulus E (GPa)	128	n	0.41
Poisson's ratio ν	0.34	α (MPa)	7.5
Density ρ (kg/m^3)	8960	β (MPa)	0.01
Specific heat c_p (J·kg^{-1}·°C^{-1})	384.6	$\dot{\varepsilon}_s$ (s^{-1})	0.001
Conductivity k (W·m^{-1}·°C^{-1})	385	$\dot{\varepsilon}_u$ (s^{-1})	10000
Taylor-Quinney coefficient Q	0.75	B (MPa)	110
σ_{y0} (MPa)	39	T_{ref} (℃)	350
A (MPa)	320	η (℃$^{-1}$)	0.0043

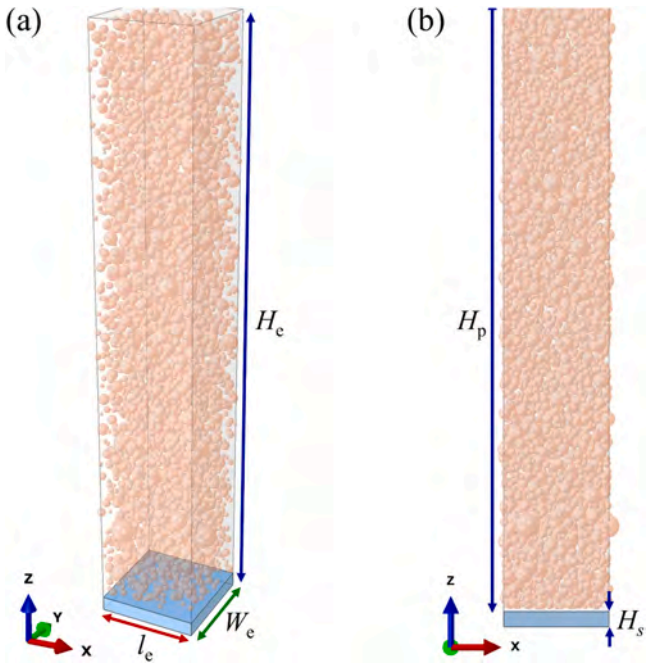

Fig. 5. Particle distribution and positioning in the Eulerian domain used for the standard Eulerian scheme: (a) isometric view and (b) x–z plane view.

The thermal-displacement analysis step was employed. Owing to the extremely short impact duration in CS, the deformation process is generally regarded as nearly adiabatic. Therefore, the temperature increase due to plastic work was incorporated through the constitutive formulation using the classical Taylor-Quinney assumption [58,59], in which a fraction of plastic dissipation is converted into heat. Meanwhile, thermal conduction was also considered to better represent realistic thermal evolution during and after impact. Although heat transfer remains limited over the short impact timescale, incorporating thermal conduction was expected to improve the physical realism of the thermomechanical response.

In the proposed framework, the first nine iterations each had a step time of 3.25×10^{-7} seconds, while the last iteration had a step time of 6×10^{-7} seconds. For the standard Eulerian scheme, the step time was set to 3.25×10^{-6} seconds. Since both the VF calculations during pre-processing and the simulation steps in the Eulerian scheme require significant computational effort, the computation times for each stage were measured separately to evaluate and compare their efficiency. All the simulations in this study were completed using a computer equipped with Intel(R) Core(TM) i7–13700 CPU@2.1 GHz and 32 GB RAM, and 16 processors with the default parallel mode were applied.

The proposed framework's accuracy was evaluated by examining the simulation at a critical stage. After the second iteration, particles started hitting the substrate. To test consistency, the results of the second iteration were compared with the beginning of the third. As shown in Fig. 6, the proposed framework reinserted the new particle batch and placed it on the top layer, and all simulation data were successfully transferred to the subsequent iteration, achieving a high-fidelity continuous multi-particle deposition simulation.

The simulation results of the proposed framework were compared with those of the standard Eulerian scheme in Fig. 7. Although the results from the two approaches are not identical due to differences in particle spatial distribution, similar surface morphologies are obtained in the 3D views shown in Fig. 7(a) and (d). This consistency mainly

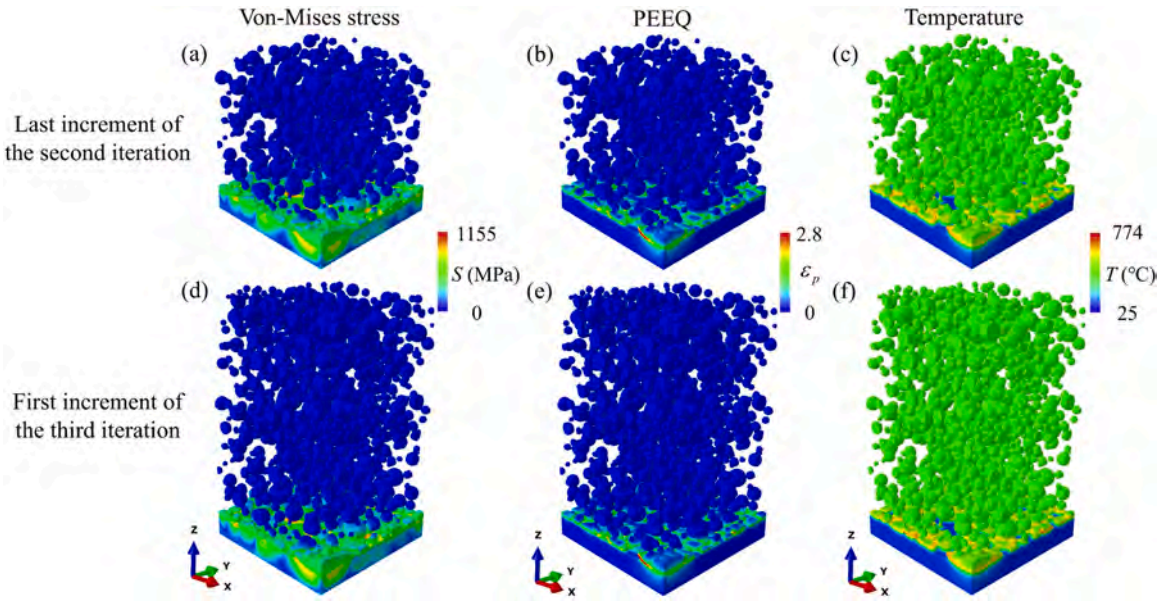

Fig. 6. Simulation results of the proposed framework: (a) von-Mises stress, (b) PEEQ and (c) temperature distributions in the last increment of the second iteration; (d) von-Mises stress, (e) PEEQ and (f) temperature distributions in the first increment of the third iteration.

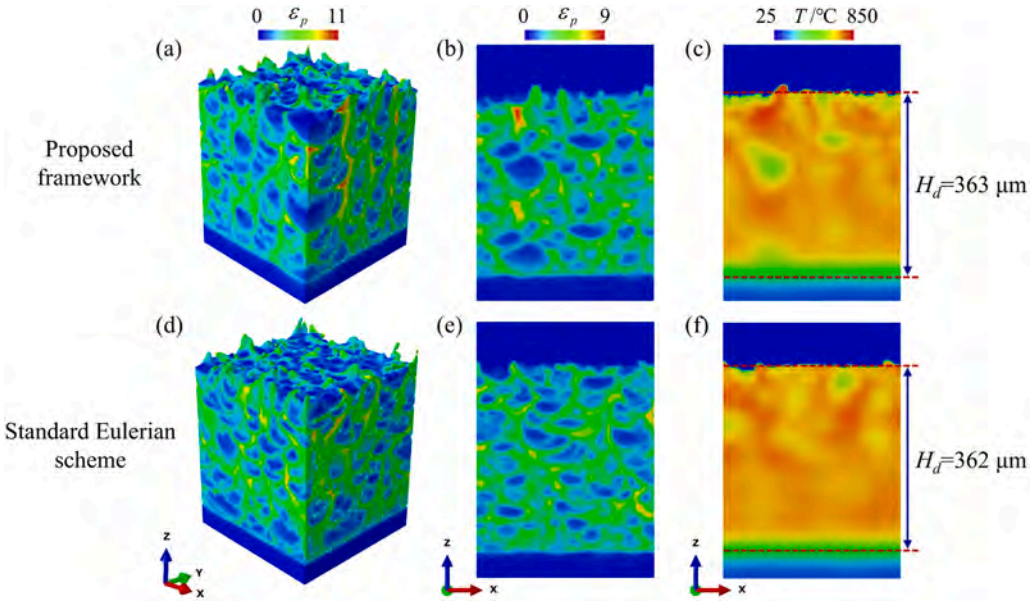

Fig. 7. Simulation results of the proposed framework: (a) PEEQ field in a 3D view; (b) PEEQ field in x-z plane side-view and (c) temperature field in x-z plane side-view. The simulation results of the standard Eulerian scheme: (d) PEEQ field in a 3D view; (e) PEEQ field in x-z plane side-view and (f) temperature field in x-z plane side-view.

resulted from both approaches employed the same Eulerian scheme and material model, leading to comparable deformation behavior and thermomechanical response during deposition. Because the boundaries of the Eulerian domain were fixed, some material collided with the boundaries after deposition, leading to reflection and intense material splashing. A 2D slice was obtained along the x-z plane. The PEEQ distributions obtained from the two approaches were quite similar, as shown in Fig. 7(b) and (e). The regions showing zero PEEQ either indicate a zero VF in the Eulerian domain or reflect relatively small PEEQ values suppressed by the contour scale. Both the temperature distribution and the deposit heights (H_d=363 μm and H_d=362 μm for the proposed framework and the standard Eulerian scheme, respectively) were also very close, as shown in Fig. 7(c) and (f). Although higher PEEQ generally corresponds to higher temperatures due to plastic dissipation, the correlation became less pronounced in lower deposit regions because thermal conduction promoted temperature uniformity over time. It should be noted that the deposits shown in Figs. 6 and 7 are not fully dense, although they may visually appear dense in the three-dimensional or cross-sectional views. A detailed discussion regarding coating porosity is provided in Section 5.3.

Finally, the computational efficiency of the two approaches was compared, in terms of computation time and RAM usage, as listed in Table 3. The reported computational time encompasses the entire workflow, including pre-processing, intermediate input-file generation, state extraction, and recurring simulation initialization. Despite accounting for these steps, the proposed framework achieved significantly

Table 3
Comparison between the computation time and RAM usage of two approaches at different stages.

Type	Proposed framework	Standard Eulerian scheme	Ratio
Element number	2737,800	9579,712	28.6%
Pre-processing time (min)	51	393	13%
Pre-processing RAM (GB)	2.3	6.7	34.3%
Executing time (min)	310	668	46.4%
Executing RAM (GB)	6.7	17	39.4%
Total time (min)	361	1061	34%

reduced computational time and RAM usage than the standard Eulerian scheme. Notably, in the pre-processing stage, the computation time for the proposed framework is just 13% of that required by the standard Eulerian scheme, as the time needed for VF calculations rises sharply with more particles. In the execution stage, the time ratio increases to 46.4%. It should be emphasized that the improved computational efficiency of the proposed framework is not achieved through an arbitrary reduction in element number or model simplification. In the standard Eulerian scheme, the computational domain must accommodate all particles, leading to a progressively larger domain and an increasing number of inactive elements after deposition. In contrast, the proposed framework maintains a compact Eulerian domain through a recurring simulation strategy, where particles leaving the placement region are replaced by newly introduced particle batches while preserving the deposition state. Therefore, the reduced number of elements is an inherent consequence of the framework design and one of its key computational advantages.

5. Experimental validation

In this section, the proposed framework is experimentally validated and used to estimate single-track deposit profiles at different scanning speeds, and also the particle flattening ratio obtained from the multi-track deposits.

5.1. Particle flow characteristics

The results of HiWatch analysis providing correlations on particle number-lateral distance, particle velocity-lateral distance, particle velocity-diameter and particle lateral velocity-lateral distance are presented in Fig. 8(a), (b), (c), and (d), respectively. To quantify the variability of the measured data, 90% scatter bars and prediction bands derived from the standard deviation are added to all fitted correlations. The relationship between particle number and lateral distance can be closely described by a Sech distribution, as presented in Fig. 8(a). This indicates that most particles are concentrated near the center, with fewer particles found toward the outer edges. Fig. 8(b) shows that particles move faster in the middle and slow down near the edges. This happens because the nozzle and airflow aren't evenly distributed, which matches the CFD results [18]. As the particle diameter increased from 10 to 85 μm, the particle velocity decreased from 625 to 580 m/s, as shown in Fig. 8(c). Although a few low-velocity outliers were observed, most particles were concentrated within the range of 550–750 m/s. The scatter may arise from tracking uncertainty or occasional airborne fine particles during measurement. The particle velocity varied quadratically with lateral distance, while particle diameter showed only a limited, approximately linear influence. Accordingly, velocity was assigned as a function of lateral position within the flow, with particles at the same position treated as having uniform velocity under the investigated processing conditions. This result is slightly different from the

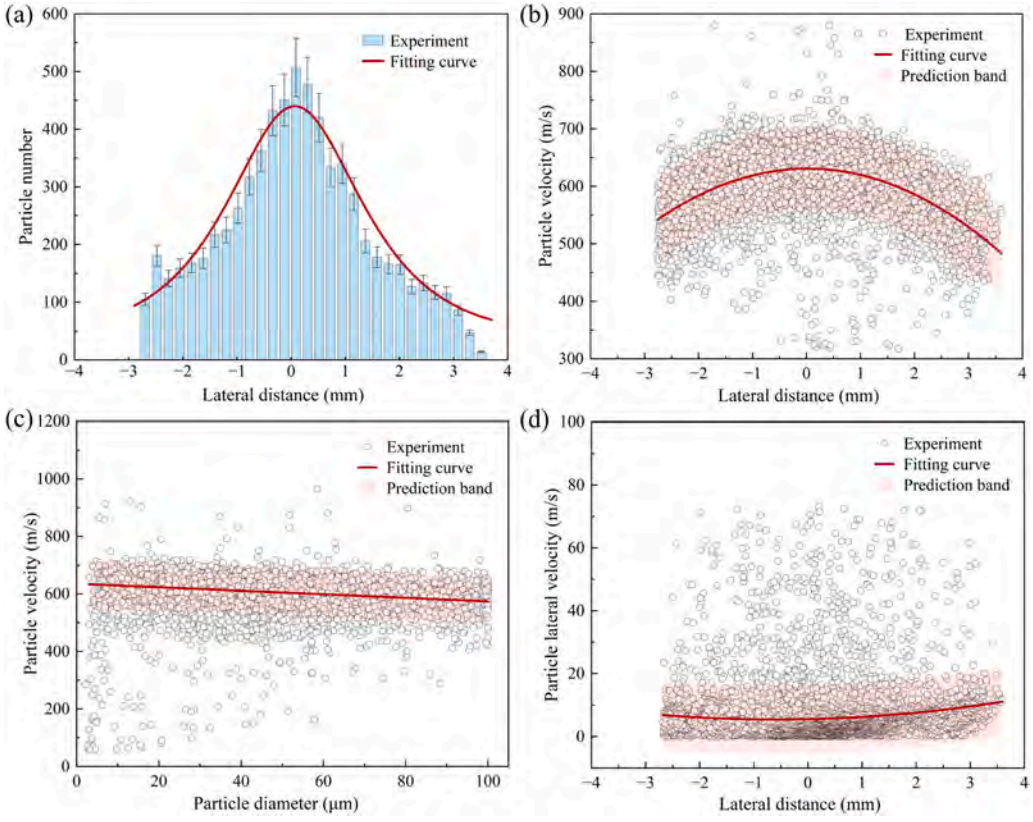

Fig. 8. The experimental in-flight particle data and the corresponding fitted curves: (a) particle number-lateral distance; (b) particle velocity-lateral distance; (c) particle velocity-diameter and (d) particle lateral velocity-lateral distance.

calculations obtained by Kinetic Spray Solutions (KSS, simulating in-flight particle parameters in CS process) [60], suggesting that the theoretical model may have simplified some particle-gas interactions. Finally, the particle lateral velocity-lateral distance data were fitted using a quadratic function, as shown in Fig. 8(d). It can be observed that the particle lateral velocities in the central region are less than those at the edges. Moreover, according to the fitted curve, the average particle lateral velocity was below 10 m/s, indicating that the influence of the lateral velocity can be neglected in the simulation.

5.2. Simulation of single-layer single-track deposition

5.2.1. Simulation setup

The particles were generated within a cylinder with a radius of approximately 3.5 mm that matches the experimental spot size. To enhance computational efficiency, the spatial and temporal scales were compressed to match real-scale conditions in terms of the number of impacting particles. From a spatial-scale perspective, assuming that the nozzle moves in a straight line at a constant velocity, the cross-sections of deposits were considered identical along the scanning paths. Therefore, to facilitate particle placement and improve computational efficiency, the circular spray domain was approximated as a rectangular region while preserving the experimentally measured particle number and velocity distributions, as shown in Fig. 9. Considering symmetry, only half of the substrate with a size of 3.55×0.3 mm^2 was simulated. The nozzle moves from the initial to the final position. During this process, the rectangular domain of the substrate was estimated to receive approximately 2.06% of the particles exiting the nozzle. The duration over which particles impact the simulated substrate can be calculated from the scanning speed to be $t = 7.3/V_s$. Subsequently, the total number of particles deposited on the simulated substrate over the entire process can be calculated based on the set feed rate, deposition duration, and particle volume, as summarized in Table 4.

Although the particle-particle gap is relatively large in the real flow, a smaller Eulerian region is preferred to reduce the computational time in the simulation [27]. In the present study, since the substrate size is fixed, the height of the particle placement region must be carefully designed to accommodate a sufficient number of particles while maintaining a realistic particle spatial distribution. The particle number distribution (Fig. 8) was measured by HiWatch under 2D conditions, and thus the experimental data can be directly adopted to prescribe the particle spatial distribution in the current simulations.

The particle impact model was established based on the assumptions shown in Fig. 9. The spatial distribution of particles and the size of the Eulerian domain are illustrated in Fig. 10(a). Particle distribution along the x-axis should follow the fitting curve of particle number-lateral distance shown in Fig. 8(a). A MATLAB script was developed to generate four different particle batches, each containing 2559 particles, with the resulting particle number distributions shown in Fig. 10(b). Therefore, 4, 6 and 8 cycles were used for the three simulations corresponding to the cases with scanning speeds of 160, 120 and 80 mm/s, as reported in Table 3, respectively. The step time of the first few iterations was 4.8×10^{-7} s, while for the last iteration it was 1.5×10^{-6} s. According to the results in Fig. 8, the particle velocity in the simulation was considered to depend only on the lateral distance from the nozzle axis, and the velocity distribution followed the fitting curve in Fig. 8(b), as shown in Fig. 10(c). l_e= 3.55 mm, W_e= 0.3 mm, H_e= 0.65 mm, H_s= 0.05 mm and H_p= 0.304 mm were used for the model. The mesh size was set to 4 μm, leading to 10,843,575 EC3D8RT elements.

Table 4
Estimated particle numbers impacting the substrate at different scanning speeds.

Sample No.	Scanning speed V_s (mm/s)	Particle number
1	160	10236
2	120	15354
3	80	20472

5.2.2. Simulation results

The fifth and eighth deposition batches for the case with a scanning speed of 80 mm/s are shown in Fig. 11(a) and (b), respectively. The particles were continuously deposited onto the substrate, eventually forming a thick coating, with the particle deformation and the simulated field data consistently transferred between successive iterations.

Comparisons between the simulated and experimental single-track deposits at different scanning speeds are shown in Fig. 12, with the experimental cross-sections deposited at scanning speeds of 80, 120 and 160 mm/s presented in Fig. 12(a), (d) and (g). The results show that deposit thickness decreased as the scanning speed increased. The thickness of the deposit at 80 mm/s was approximately twice that at 160 mm/s, which is consistent with previous studies [22,44]. The simulated deposits at scanning speeds of 80, 120 and 160 mm/s shown in Fig. 12(b), (e) and (h), indicate a good agreement with the experimental cross-sectional profiles, exhibiting a slightly higher center and lower edges, which indicates that the particle spatial distribution applied in simulations successfully reproduces the experimental measurements. The surface profiles and cross-sections of the deposits obtained from the simulations were compared with experimental 2D and 3D data for deposits sprayed at scanning speeds of 80, 120 and 160 mm/s in Fig. 12(c), (f), and (i). The results show that the proposed framework can accurately reproduce the experimental deposits profiles, highlighting its strong predictive capability.

The maximum heights and overlapping ratios of the simulated and experimental deposits were further obtained for quantitative comparison, as shown in Fig. 13(a) and (b). The maximum heights of the

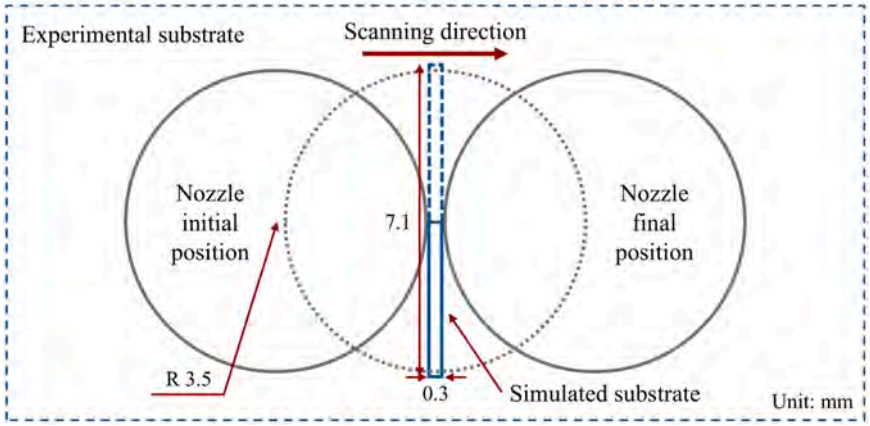

Fig. 9. The size and position of the simulated substrate relative to those of the moving nozzle.

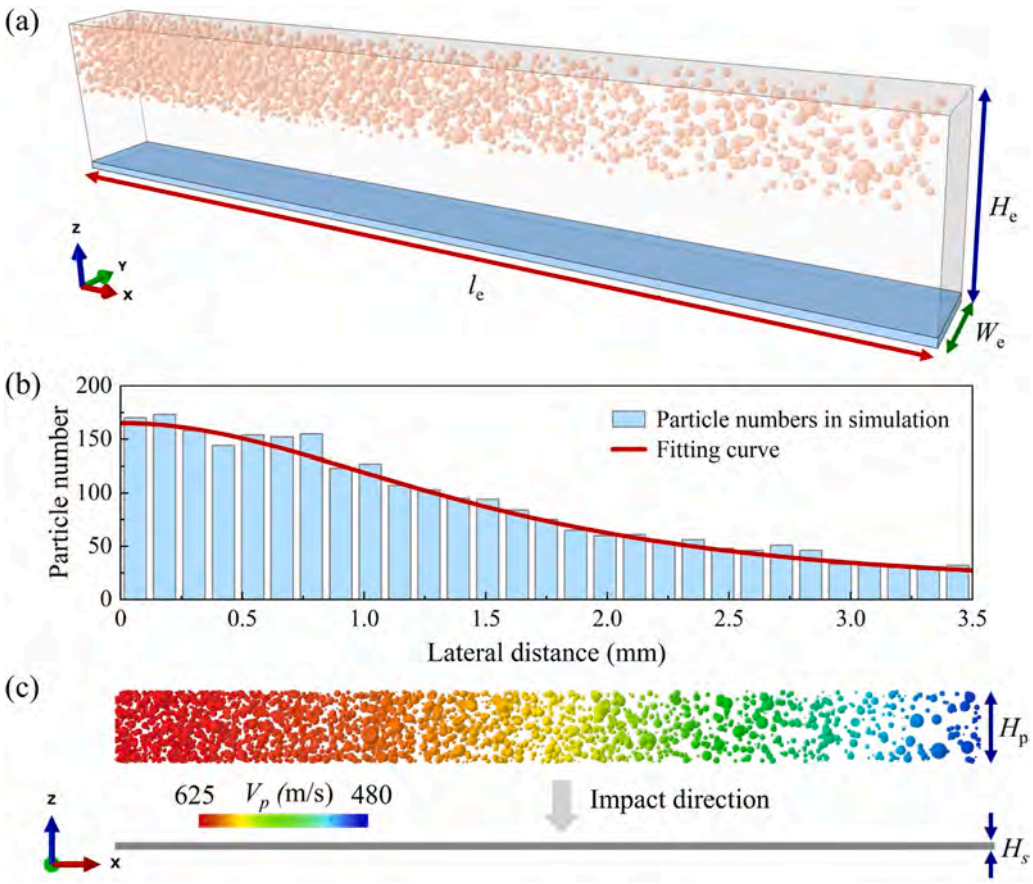

Fig. 10. The model for single track deposition simulation: (a) particle spatial distribution within the flow; (b) particle number distribution within the flow and (c) particle velocity distribution within the flow.

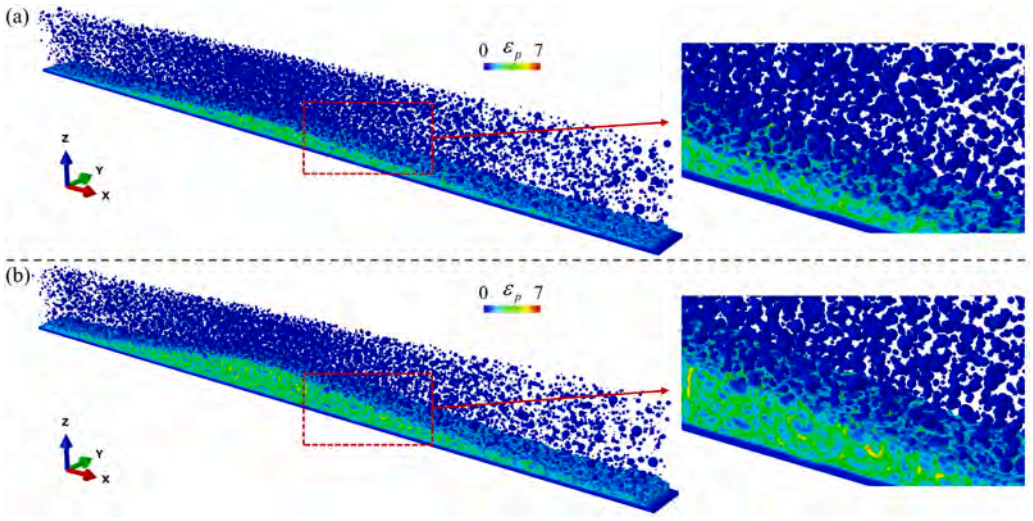

Fig. 11. The (a) fifth and (b) eighth deposition processes at a scanning speed of 80 mm/s.

simulated and experimental deposits are nearly identical at different scanning speeds, and the maximum deviation between the two is 2.2% at a scanning speed of 160 mm/s. The overlapping ratios remain above 80% for all scanning speeds, with a higher overlapping ratio observed at the lowest examined scanning speed. This may be attributed to the assumption that the circular deposition region was simplified to a rectangular shape. Such assumption may slightly alter the particle distribution near the edge regions, particularly at higher scanning speeds where the deposited track becomes narrower, thereby affecting the overlapping ratio. Nevertheless, the overall deposit morphology and thickness remain in good agreement with the experiments.

The local surface features of the deposits at a scanning speed of 120 mm/s were extracted from both the experiments and simulations for analysis, as shown in Fig. 14. The simulations successfully captured the surface morphology and roughness, showing good agreement with the experimentally observed local surface characteristics.

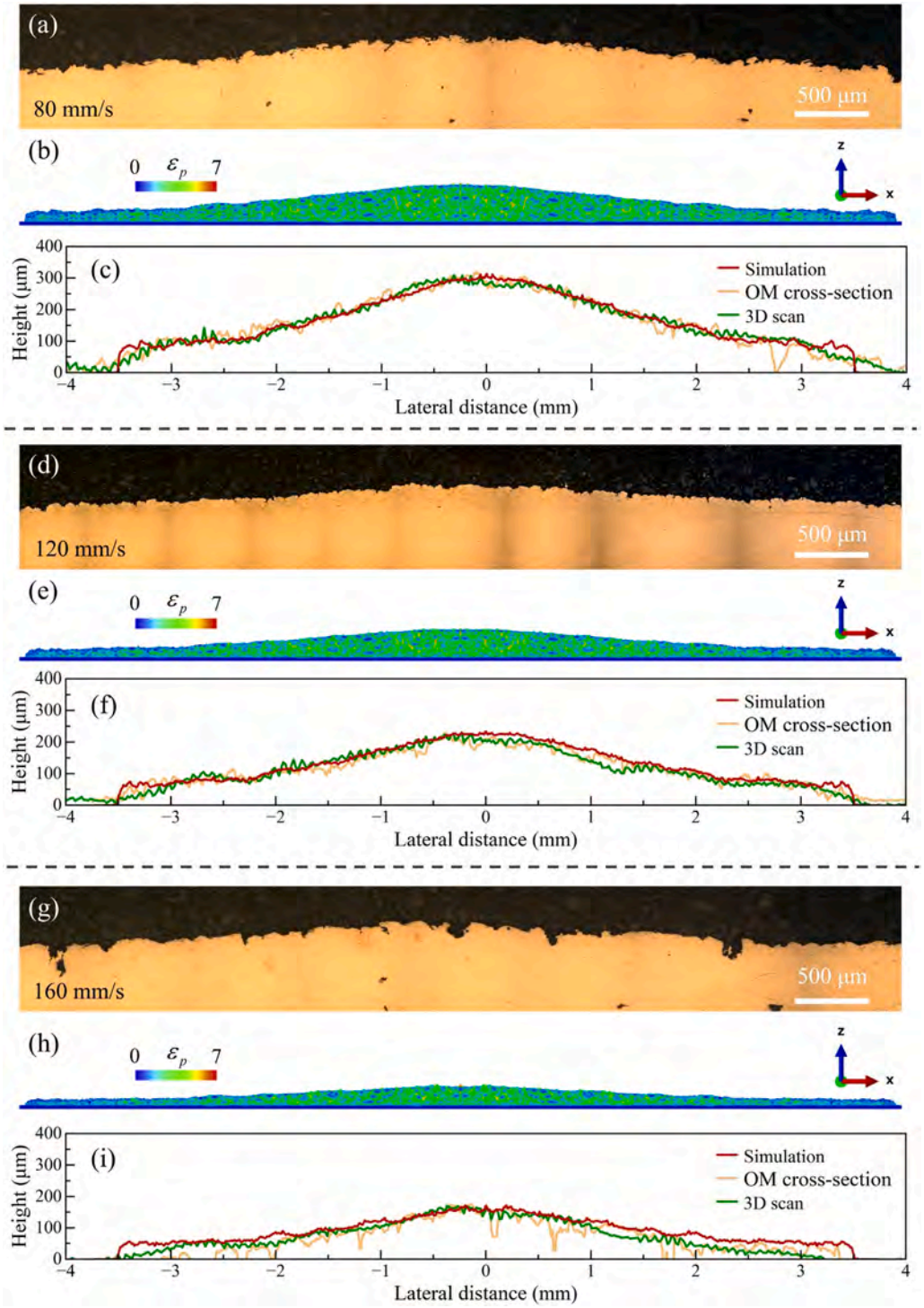

Fig. 12. Comparison between simulated and experimental deposits: (a) experimental OM cross-section, (b) simulated deposit and (c) surface profiles at scanning speed of 80 mm/s; (d) experimental OM cross-section, (e) simulated deposit and (f) surface profiles at scanning speed of 120 mm/s; (g) experimental OM cross-section, (h) simulated deposit and (i) surface profiles at scanning speed of 160 mm/s.

Meanwhile, the surface features of the deposits obtained from both the 3D scans and simulations were extracted and processed using Gaussian filtering to obtain the average surface profile. Subsequently, the two standard roughness parameters of arithmetic mean roughness (R_a) and the root mean square roughness (R_q) [61] were employed to quantify the surface roughness; the results are presented in Fig. 15. The maximum discrepancy between the simulation and experimental results was observed at a scanning speed of 160 mm/s when evaluated using the R_a parameter, with a relative error of 13%. Overall, the predicted surface roughness agrees well with the experimental data. However, the simulated values were slightly underestimated, primarily due to the coarse mesh resolution, which restricts the accurate representation of individual particle deformation. Owing to the application of a high-fidelity multi-particle impact model together with the accurate Ge material model, the simulation can accurately reproduce the deformation behavior of the deposits from the global to the local scale.

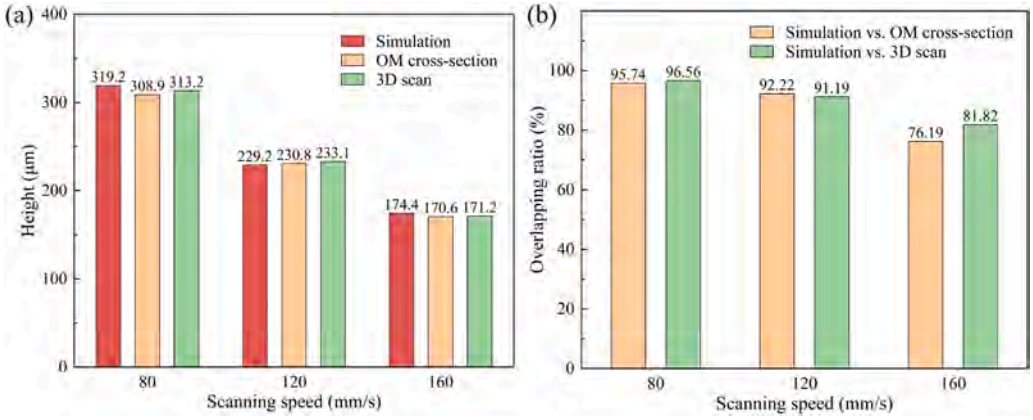

Fig. 13. Quantitative comparison between simulated and experimental deposits: (a) maximum heights and (b) profile overlapping ratios.

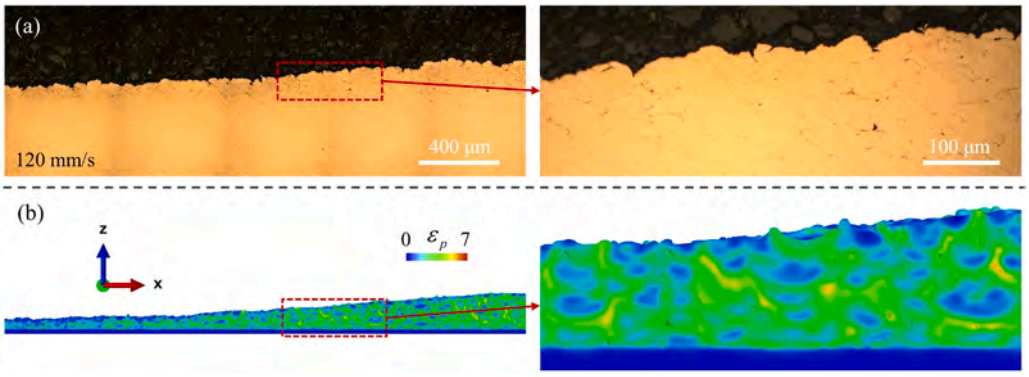

Fig. 14. The local surface characteristics of (a) experimental and (b) simulated deposits at a scanning speed of 120 mm/s.

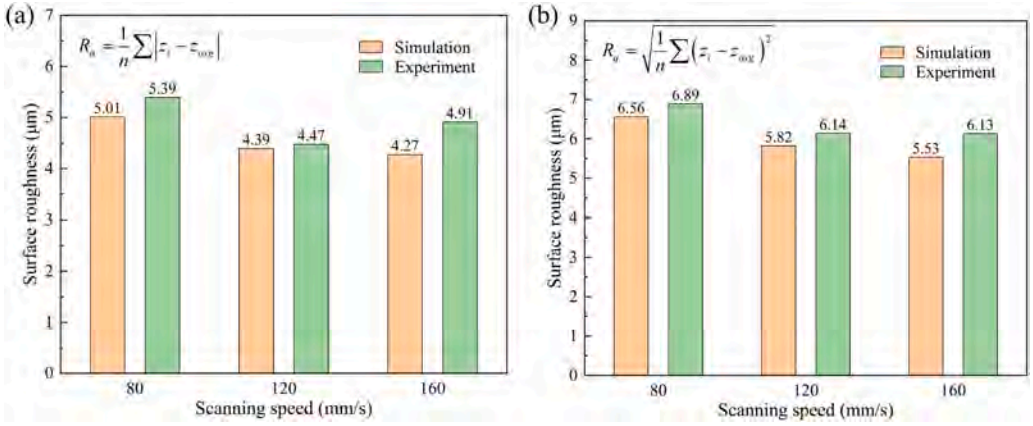

Fig. 15. Experimental and simulated surface roughness parameters (a) R_a and (b) R_q.

5.3. Simulation of multi-layer multi-track deposition

In the multi-layer multi-track simulation, all parameters and particle spatial distributions were identical to those applied in Section 4, with only the mesh size further refined to 2 μm to achieve higher simulation accuracy, leading to 9187,500 EC3D8RT elements in the model.

The cross-sectional microstructures of the experimental and simulated deposits were compared in Fig. 16. Because particle boundaries cannot be explicitly tracked in the Eulerian scheme, the PEEQ field was used as an approximate indicator of these boundaries. Impact-induced plastic deformation generally produces localized PEEQ concentrations near particle interfaces; therefore, particle boundaries were identified qualitatively from PEEQ localization without applying a specific threshold. To facilitate visualization and comparison with experiments, image contrast enhancement was applied during post-processing to improve boundary visibility, as shown in Fig. 16(b). Consequently, some discrepancies between the experimental and simulated deformation gradients are expected because of the approximate boundary definition, although the overall deformation trend was captured. Overall, the simulation successfully reproduced the key aspects of particle deformation and stacking characteristics observed in the experiments. Subsequently, the polished cross-sectional microstructure and simulated VF field were extracted for porosity comparison, as shown in Fig. 16(c) and (d), respectively. In the Eulerian scheme, the VF field represents local

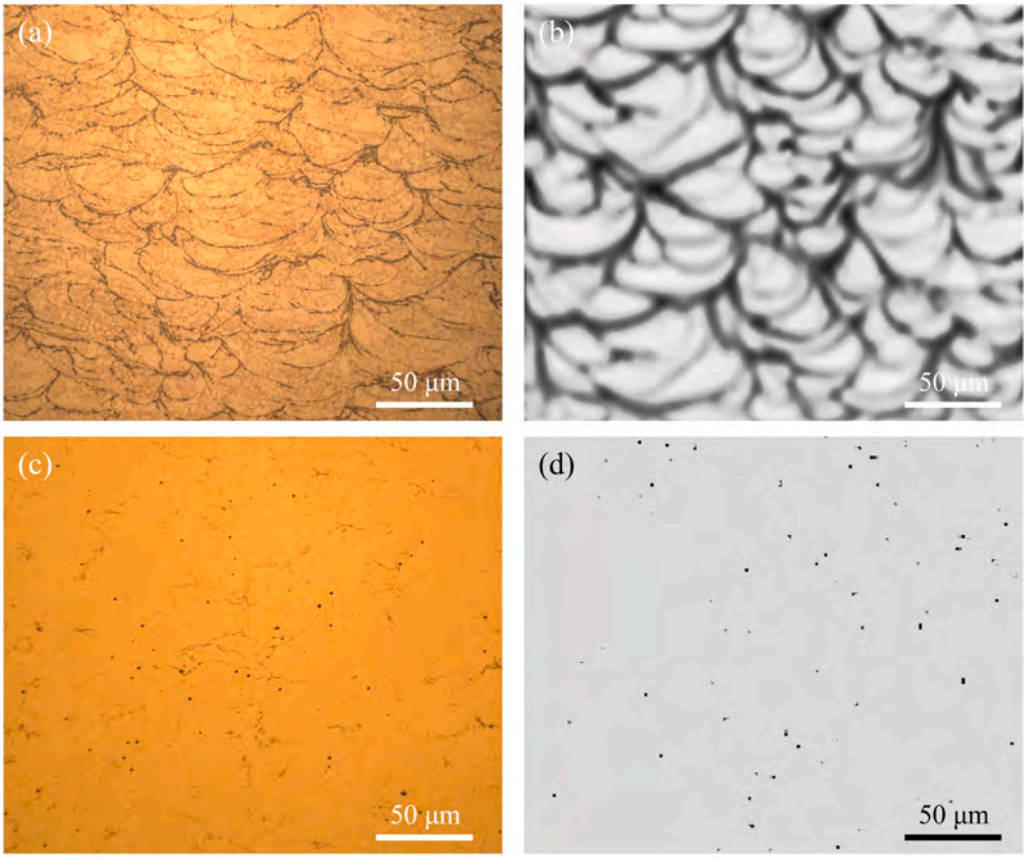

Fig. 16. Cross-sectional micrographs of the multi-track deposits from: (a) etched microstructure, (b) simulated particle interfaces, (c) polished microstructure, and (d) simulated VF field.

material occupancy, where regions with reduced or zero VF can be interpreted as pores [28]. ImageJ software was used to quantify the porosity, yielding values of 0.31% and 0.53% for the experimental and simulated results, respectively. The relatively low porosity was attributed to the selected spraying parameters, which is consistent with the previous study [57]. The proposed framework reasonably predicted the deposit porosity. Although the simulated porosity is slightly higher than the experimental one, a finer mesh size is expected to further improve the prediction accuracy.

To calculate the flattening ratio, particles with clearer boundaries were selected from the cross-sections in both the experimental and simulated deposits. Two methods were adopted to evaluate the particle flattening ratio. The first one is based on the width W_p and height H_p of the deformed particles [62–64]:

$$\text{Flatteningratio} = W_p/H_p \tag{5}$$

However, this method does not consider the original particle size and therefore does not directly evaluate the shape change [65]. The second method incorporates the original particle diameter D [66,67], but since the original diameter cannot be obtained in experiments, and it was estimated based on volume conservation [68]:

$$\text{Flatteningratio} = W_p/D \quad \text{with} \quad D = \sqrt[3]{W_p^2 H_p} \tag{6}$$

The flattening ratios calculated by Eqs. (5) and (6) are shown in Fig. 17(a) and (b), respectively. Linear regression with 90% confidence

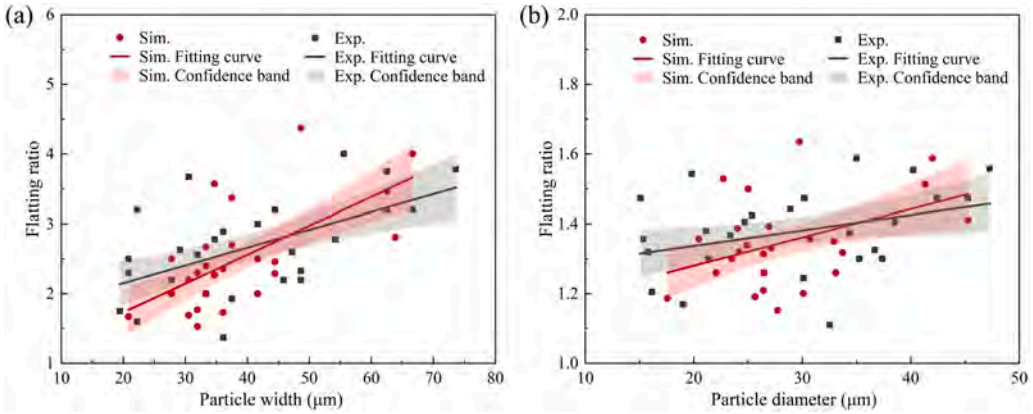

Fig. 17. Experimental and simulated flattening ratios calculated using the two approaches described in (a) Eq. (5) and (b) Eq. (6).

bands was employed to highlight the overall tendency of the data and quantify the associated uncertainty. Although noticeable scatter exists, the observed tendency remains meaningful for comparative interpretation between experimental and simulation results. According to the fitting curves, the flattening ratio increased with increasing deformed particle's width. Interestingly, the flattening ratio also increased with the original particle diameter, although the increase was relatively small, from approximately 1.2–1.4. This may be attributed to the fact that in multi-particle impact cases, larger particles are more susceptible to successive impacts, leading to a more severe flattening. Overall, the proposed framework can accurately reproduce the deformation behavior of multi-particle impact, demonstrating its reliability and potential for the quantitative analysis of particle-scale deformation mechanisms in the CS deposition process.

6. Conclusions

In this study, we develop a high-fidelity open-source multi-particle impact framework to solve real-scale CS deposition problems. This framework employed an automated recurring simulation strategy to significantly reduce computational costs, leveraging the strengths of Eulerian simulations. It also incorporated a high-precision material model to accurately capture particle deformations. The computational efficiency of the proposed framework was evaluated by comparing it with the standard Eulerian scheme, and its accuracy was validated against experimental results obtained using various spraying parameters. The results demonstrated that the combination of the proposed recurring simulation strategy, the constitutive model, and the Eulerian scheme enable a reliable prediction of various deposit features. Such capability makes the proposed framework a valuable tool for spray parameter optimization and practical process design in CSAM. The main conclusions of this study are as follows:

(1) The proposed framework successfully simulated large-scale CS deposition and accurately captured deposit characteristics both qualitatively and quantitatively, including overall profiles, surface roughness, cross-sectional particle flattening ratios, and porosity.
(2) The proposed recurring simulation strategy overcame the inherent limitations of current integration of Eulerian scheme in Abaqus by automatically calculating volume fractions and generating the corresponding sets during the pre-processing stage, while ensuring efficient and robust data transfer throughout the execution stage.
(3) The proposed high-precision material model enabled accurate prediction of both global and local deformation behavior in large-scale multi-particle simulations, highlighting its important role in connecting particle-scale mechanism with overall deposit formation.
(4) Compared with the standard Eulerian scheme, the proposed framework maintained accuracy while reducing computational time and memory usage up to 34% and 35%, respectively, making ten-million-element CS simulations feasible on personal computers.

CRediT authorship contribution statement

Xuanyu Ge: Writing – original draft, Validation, Software, Methodology, Conceptualization. **Linglong Zhou:** Validation, Software, Data curation. **Amir Ardeshiri Lordejani:** Writing – review & editing, Investigation. **Asghar Heydari Astaraee:** Writing – review & editing, Investigation. **Sara Bagherifard:** Writing – review & editing, Supervision, Resources. **Mario Guagliano:** Writing – review & editing, Supervision, Resources.

Declaration of Generative AI and AI-assisted technologies in the writing process

Microsoft copilot was used during the writing of this manuscript solely for language editing to improve grammar and clarity. The tool did not generate scientific content, data analysis, interpretations, or conclusions. All scientific content was generated, written, reviewed, and verified by the authors. The authors accept full responsibility for the content of the manuscript.

Declaration of Competing Interest

The authors declare that they have no known competing financial interests or personal relationships that could have appeared to influence the work reported in this paper.

Acknowledgments

X.G. acknowledges the Chinese Scholarship Council (CSC) for the financial support (No. 202306290021). L.Z. acknowledges the Chinese Scholarship Council (CSC) for the financial support (No. 202406290022). Authors acknowledge ArcHIDep funding from the European Research Council (ERC) under grant agreement n. 101044228. Views and opinions expressed are, however, those of the authors only and do not necessarily reflect those of the European Union or the European Research Council Executive Agency. Neither the European Union nor the granting authority can be held responsible for them.

Appendix A. Methodological clarification

The proposed framework involves several numerical and physical considerations that require further clarification. The mesh sizes adopted in different sections were selected by balancing numerical accuracy, physical domain scale, and computational feasibility. Since finer meshes generally improve the particle deformation resolution in Eulerian simulations while significantly increasing memory consumption, the total element number in the present study was practically limited to approximately ten million elements due to the available computational hardware. Accordingly, Sections 4, 5.2.1, and 5.3 employed approximately 9.58, 10.84, and 9.19 million elements, corresponding to mesh sizes of 4, 3, and 2 μm, respectively. Therefore, the variation in mesh size reflects differences in simulation scale and computational demand rather than inconsistencies in the modeling strategy.

Several physical assumptions adopted in the present framework should also be clarified. First, no explicit adhesion criterion was imposed, and particle bonding in the Eulerian scheme followed the inherent material continuity treatment during impact, effectively assuming complete particle deposition. Second, material jetting and localized adiabatic shear instability, both of which are commonly associated with bonding in CS, have previously been reproduced in validated single-particle simulations employing the same constitutive model and Eulerian scheme [55]. Accordingly, these mechanisms are preserved in the present framework, while oxide disruption is not modeled. Third, the present framework effectively assumed complete particle deposition, while sub-critical particle rebound was not modeled. This simplification mainly originated from the default Eulerian contact treatment in Abaqus, where selective deposition and rebound behavior are difficult to implement. Consequently, effects associated with incomplete deposition, such as partially deformed or undeformed embedded particles and peening-induced densification, were not resolved in the current framework. Since the primary objective of this study is to investigate deposit morphology and evolution under continuous multi-particle impact conditions, these simplifications were considered acceptable.

Within these assumptions, the applicability and scalability of the

proposed framework should also be discussed. Although validated using Cu, the framework is not material-specific and can be extended to other materials through appropriate constitutive models [49,50,55]. Moreover, while developed within an Eulerian scheme, the recurring strategy can also be extended to the widely used CEL approaches [27–29,31–33]. The present framework demonstrated recurring simulations involving approximately 20,000 particles on a personal computer and is not inherently limited by the particle number, as additional particles can be introduced through successive recurring cycles while maintaining a nearly constant computational domain size. Larger deposition domains mainly require additional recurring cycles, thereby increasing the computational time without altering the operating mechanism of the proposed strategy. Although the present simulations were constrained by the available computational hardware, the framework can be extended to larger-scale CS simulations on high-performance computing platforms. Furthermore, Section 4 demonstrated comparable deposition behavior between the proposed framework and the standard Eulerian scheme, indicating negligible numerical artifacts introduced by recurring cycles under the investigated conditions.

Data availability

I have shared the link to my codes.

References

[1] H. Assadi, H. Kreye, F. Gärtner, T. Klassen, Cold spraying-A materials perspective, Acta Mater. 116 (2016) 382–407.
[2] W. Li, K. Yang, S. Yin, X. Yang, Y. Xu, R. Lupoi, Solid-state additive manufacturing and repairing by cold spraying: a review, J. Mater. Sci. Technol. 34 (2018) 440–457.
[3] W. Li, C. Cao, S. Yin, Solid-state cold spraying of Ti and its alloys: a literature review, Prog. Mater. Sci. 110 (2020) 100633.
[4] S. Yin, P. Cavaliere, B. Aldwell, R. Jenkins, H. Liao, W. Li, R. Lupoi, Cold spray additive manufacturing and repair: fundamentals and applications, Addit. Manuf. 21 (2018) 628–650.
[5] S. Bagherifard, J. Kondas, S. Monti, J. Cizek, F. Perego, O. Kovarik, F. Lukac, F. Gaertner, M. Guagliano, Tailoring cold spray additive manufacturing of steel 316 L for static and cyclic load-bearing applications, Mater. Des. 203 (2021) 109575.
[6] S. Bagherifard, A. Heydari Astaraee, M. Locati, A. Nawaz, S. Monti, J. Kondás, R. Singh, M. Guagliano, Design and analysis of additive manufactured bimodal structures obtained by cold spray deposition, Addit. Manuf. 33 (2020) 101131.
[7] R.A. Wicaksono, A.Ardeshiri Lordejani, S. Bagherifard, Current trends and future perspective for cold spray metal-ceramic composites, Adv. Eng. Mater. 27 (2025) 2401657.
[8] C. Schillaci, D. Pilone, F. Berto, C. Bellini, V. Di Cocco, P. Di Giamberardino, D. Iacoviello, Correlation between process parameters and mechanical properties of ti6al4v alloys processed by electron beam melting, Fract. Struct. Integr. 19 (74) (2025) 310–320.
[9] S. Yin, N. Fan, C. Huang, Y. Xie, C. Zhang, R. Lupoi, W. Li, Towards high-strength cold spray additive manufactured metals: methods, mechanisms, and properties, J. Mater. Sci. Technol. 170 (2024) 47–64.
[10] P. Poza, M.Á. Garrido-Maneiro, Cold-sprayed coatings: microstructure, mechanical properties, and wear behaviour, Prog. Mater. Sci. 123 (2022) 100839.
[11] S. Bagherifard, S. Monti, M.V. Zuccoli, M. Riccio, J. Kondás, M. Guagliano, Cold spray deposition for additive manufacturing of freeform structural components compared to selective laser melting, Mater. Sci. Eng. A 721 (2018) 339–350.
[12] S. Bagherifard, M. Guagliano, Fatigue performance of cold spray deposits: coating, repair and additive manufacturing cases, Int. J. Fatigue 139 (2020) 105744.
[13] R. Falco, S. Bagherifard, Cold spray additive manufacturing: a review of shape control challenges and solutions, J. Therm. Spray. Technol. 34 (4) (2025) 1023–1041.
[14] S.E. Julien, A. Nourian-Avval, W. Liang, T. Schwartz, O.C. Ozdemir, S. Müftü, Bulk fracture anisotropy in cold-sprayed Al 6061 deposits, Eng. Fract. Mech. 263 (2022) 108301.
[15] G. Prashar, H. Vasudev, A comprehensive review on sustainable cold spray additive manufacturing: state of the art, challenges and future challenges, J. Clean. Prod. 310 (2021) 127606.
[16] B. Mahato, J. Yoder, G. Simmons, N. Huft, I. Nault, P. Lucon, Particle dynamics in low-pressure cold spray additive manufacturing-A numerical and experimental study, Addit. Manuf. 110 (2025) 104937.
[17] R.N. Raoelison, Role of the Magnus effect in additive manufacturing at the scale of the micron-sized powders within the supersonic gas flow of cold spraying, Addit. Manuf. 97 (2025) 104610.
[18] C. Xing, W. Li, Y. Xu, C. Huang, A novel three-dimensional profile prediction method integrated with particle acceleration simulation and layer stacking in cold spray additive manufacturing, Addit. Manuf. 109 (2025) 104866.
[19] H. Wu, X. Xie, M. Liu, C. Chen, H. Liao, Y. Zhang, S. Deng, A new approach to simulate coating thickness in cold spray, Surf. Coat. Technol. 382 (2020) 125151.
[20] D. Vanerio, J. Kondas, M. Guagliano, S. Bagherifard, 3D modelling of the deposit profile in cold spray additive manufacturing, J. Manuf. Process. 67 (2021) 521–534.
[21] A. Ardeshiri Lordejani, L. Romanenghi, A. Pollastri, M. Guagliano, S. Bagherifard, Deposit shape control for local repair and welding by cold spray, J. Manuf. Process. 112 (2024) 45–59.
[22] R. Falco, M. Jalayer, S. Bagherifard, Enhanced geometrical control in cold spray additive manufacturing through deep neural network predictive models, Virtual Phys. Prototyp. 20 (1) (2025) e2472388.
[23] A. Fardan, C.C. Berndt, R. Ahmed, Numerical modelling of particle impact and residual stresses in cold sprayed coatings: a review, Surf. Coat. Technol. 409 (2021) 126835.
[24] S. Yin, X. Wang, X. Suo, H. Liao, Z. Guo, W. Li, C. Coddet, Deposition behavior of thermally softened copper particles in cold spraying, Acta Mater. 61 (14) (2013) 5105–5118.
[25] P.C. King, G. Bae, S.H. Zahiri, M. Jahedi, C. Lee, An experimental and finite element study of cold spray copper impact onto two aluminum substrates, J. Therm. Spray. Technol. 19 (3) (2010) 620–634.
[26] X. Ge, Y. Ma, L. Zhou, W. Li, Modelling the anisotropic fracture behaviour of cold spray additive manufactured 6061 aluminium alloy deposits based on the phase field method, Addit. Manuf. 79 (2024) 103932.
[27] A.Ardeshiri Lordejani, D. Colzani, M. Guagliano, S. Bagherifard, An inclusive numerical framework to assess the role of feedstock features on the quality of cold spray deposits, Mater. Des. 224 (2022) 111374.
[28] S. Weiller, F. Delloro, A numerical study of pore formation mechanisms in aluminium cold spray coatings, Addit. Manuf. 60 (2022) 103193.
[29] W. Li, K. Yang, D. Zhang, X. Zhou, Residual stress analysis of cold-sprayed copper coatings by numerical simulation, J. Therm. Spray. Technol. 25 (1) (2016) 131–142.
[30] W. Li, H. Liao, C. Li, G. Li, C. Coddet, X. Wang, On high velocity impact of micro-sized metallic particles in cold spraying, Appl. Surf. Sci. 253 (5) (2006) 2852–2862.
[31] F. Wang, W. Li, M. Yu, H. Liao, Prediction of critical velocity during cold spraying based on a coupled thermomechanical Eulerian model, J. Therm. Spray. Technol. 23 (1) (2014) 60–67.
[32] M. Yu, W. Li, F. Wang, H. Liao, Finite element simulation of impacting behavior of particles in cold spraying by Eulerian approach, J. Therm. Spray. Technol. 21 (3) (2012) 745–752.
[33] W. Li, K. Yang, S. Yin, X. Guo, Numerical analysis of cold spray particles impacting behavior by the Eulerian method: a review, J. Therm. Spray. Technol. 25 (8) (2016) 1441–1460.
[34] W. Li, S. Yin, X. Wang, Numerical investigations of the effect of oblique impact on particle deformation in cold spraying by the SPH method, Appl. Surf. Sci. 256 (12) (2010) 3725–3734.
[35] B. Gnanasekaran, G. Liu, Y. Fu, G. Wang, W. Niu, T. Lin, A smoothed particle hydrodynamics (SPH) procedure for simulating cold spray process-a study using particles, Surf. Coat. Technol. 377 (2019) 124812.
[36] S. Rahmati, A. Zúñiga, B. Jodoin, R.G.A. Veiga, Deformation of copper particles upon impact: A molecular dynamics study of cold spray, Comput. Mater. Sci. 171 (2020) 109219.
[37] L.M. Pereira, A. Zúñiga, B. Jodoin, R.G.A. Veiga, S. Rahmati, Unraveling jetting mechanisms in high-velocity impact of copper particles using molecular dynamics simulations, Addit. Manuf. 75 (2023) 103755.
[38] F. Chen, W. Yan, High-fidelity modelling of thermal stress for additive manufacturing by linking thermal-fluid and mechanical models, Mater. Des. 196 (2020) 109185.
[39] L. Liang, R. Hu, J. Wang, A. Huang, S. Pang, A thermal fluid mechanical model of stress evolution for wire feeding-based laser additive manufacturing, J. Manuf. Process. 69 (2021) 602–612.
[40] M. Bayat, V.K. Nadimpalli, F.G. Biondani, S. Jafarzadeh, J. Thorborg, N.S. Tiedje, G. Bissacco, D.B. Pedersen, J.H. Hattel, On the role of the powder stream on the heat and fluid flow conditions during directed energy deposition of maraging steel-Multiphysics modeling and experimental validation, Addit. Manuf. 43 (2021) 102021.
[41] X. Lai, G. Yang, Y. Wang, Z. Wei, Heat and mass transfer in electron beam additive manufacturing, Int. J. Mech. Sci. 259 (2023) 108613.
[42] G. Bolelli, S. Dosta, L. Lusvarghi, T. Manfredini, J.M. Guilemany, I.G. Cano, Building up WC-Co coatings by cold spray: A finite element simulation, Surf. Coat. Technol. 374 (2019) 674–689.
[43] M. Hassani-Gangaraj, D. Veysset, V.K. Champagne, K.A. Nelson, C.A. Schuh, Adiabatic shear instability is not necessary for adhesion in cold spray, Acta Mater. 158 (2018) 430–439.
[44] Z. Zhang, D. Gitardi, M. Scarafile, A. Valente, M. Afrasiabi, M. Bambach, Experimental and numerical investigations of pore formation mechanisms in cold spray, J. Manuf. Process. 127 (2024) 488–510.
[45] X. Ge, L. Zhou, S. Bagherifard, M. Guagliano, A simple and efficient implementation of explicit phase field method in ABAQUS to address complex three-dimensional fracture problems, Eng. Fract. Mech. 323 (2025) 111222.
[46] S. Sayahlatifi, Z. Zaiemyekeh, C. Shao, A. McDonald, J.D. Hogan, Strain rate-dependent behavior of cold-sprayed additively manufactured Al-Al2O3 composites: Micromechanical modeling and experimentation, Compos. Part. B Eng. 280 (2024) 111479.
[47] Y. Ying, Y. Feng, W. Huang, X. Yao, A thermo-mechanical phase field fracture model considering solid–liquid transition, Eng. Fract. Mech. 338 (2026) 112025.

[48] X. Ge, L. Zhou, Y. Ying, S. Bagherifard, M. Guagliano, Combining phase field method and critical distance theory for predicting fatigue life of notched specimens, Int. J. Mech. Sci. 282 (2024) 109608.
[49] G.R. Johnson, W.H. Cook, Fracture characteristics of three metals subjected to various strains, strain rates, temperatures and pressures, Eng. Fract. Mech. 21 (1) (1985) 31–48.
[50] Q. Wang, N. Ma, M. Takahashi, X. Luo, C. Li, Development of a material model for predicting extreme deformation and grain refinement during cold spraying, Acta Mater. 199 (2020) 326–339.
[51] Q. Wang, N. Ma, X. Luo, C. Li, Towards better understanding supersonic impact-bonding behavior of cold sprayed 6061-T6 aluminum alloy based on a high-accuracy material model, Addit. Manuf. 48 (2021) 102469.
[52] R. Chakrabarty, J. Song, A modified Johnson-Cook material model with strain gradient plasticity consideration for numerical simulation of cold spray process, Surf. Coat. Technol. 397 (2020) 125981.
[53] Y. Cormier, P. Dupuis, B. Jodoin, A. Ghaei, Finite element analysis and failure mode characterization of pyramidal fin arrays produced by masked cold gas dynamic spray, J. Therm. Spray. Technol. 24 (8) (2015) 1549–1565.
[54] J. Henao, G. Bolelli, A. Concustell, L. Lusvarghi, S. Dosta, I.G. Cano, J. M. Guilemany, Deposition behavior of cold-sprayed metallic glass particles onto different substrates, Surf. Coat. Technol. 349 (2018) 13–23.
[55] X. Ge, L. Zhou, S. Bagherifard, M. Guagliano, High-Fidelity modeling of cold spray: Improved constitutive material model and nonlocal mesh sensitivity mitigation, Int. J. Mech. Sci. 321 (2026) 111654.
[56] W. Li, J. Yang, Z. Zhang, Y. Xie, C. Huang, High ductility induced by twin-assisted grain rotation and merging in solid-state cold spray additive manufactured Cu, J. Mater. Sci. Technol. 214 (2025) 11–15.
[57] F. Zarei, A.Ardeshiri Lordejani, S. Ruan, S. Yin, M. Guagliano, R. Lupoi, S. Bagherifard, Evaluating the Application of Cold Spray Technology for the Deposition of Copper–Graphene Composite Coatings, Coatings 15 (2025) 153.
[58] G.C. Soares, M. Hokka, The Taylor–Quinney coefficients and strain hardening of commercially pure titanium, iron, copper, and tin in high rate compression, Int. J. Impact Eng. 156 (2021) 103940.
[59] S.D. Salehi, O. Kingstedt, Critical assessment and demonstration of high-emissivity coatings for improved infrared signal quality for Taylor–Quinney coefficient experimentation, Int. J. Impact Eng. 178 (2023) 104593.
[60] T. Schmidt, H. Assadi, F. Gärtner, H. Richter, T. Stoltenhoff, H. Kreye, T. Klassen, From particle acceleration to impact and bonding in cold spraying, J. Therm. Spray. Technol. 18 (5) (2009) 794–808.
[61] A. Bruera, P. Puddu, S. Theimer, M. Villa-Vidaller, A. List, G. Bolelli, F. Gärtner, T. Klassen, L. Lusvarghi, Adhesion of cold sprayed soft coatings: Effect of substrate roughness and hardness, Surf. Coat. Technol. 466 (2023) 129651.
[62] N.H. Tariq, L. Gyansah, J.Q. Wang, X. Qiu, B. Feng, M.T. Siddique, T.Y. Xiong, Cold spray additive manufacturing: A viable strategy to fabricate thick B4C/Al composite coatings for neutron shielding applications, Surf. Coat. Technol. 339 (2018) 224–236.
[63] X. Chu, R. Chakrabarty, H. Che, L. Shang, P. Vo, J. Song, S. Yue, Investigation of the feedstock deposition behavior in a cold sprayed 316L/Fe composite coating, Surf. Coat. Technol. 337 (2018) 53–62.
[64] X. Chu, H. Che, C. Teng, P. Vo, S. Yue, A multiple particle arrangement model to understand cold spray characteristics of bimodal size 316L/Fe powder mixtures, Surf. Coat. Technol. 381 (2020) 125137.
[65] A.A. Tiamiyu, C.A. Schuh, Particle flattening during cold spray: Mechanistic regimes revealed by single particle impact tests, Surf. Coat. Technol. 403 (2020) 126386.
[66] H. Assadi, F. Gärtner, T. Stoltenhoff, H. Kreye, Bonding mechanism in cold gas spraying, Acta Mater. 51 (15) (2003) 4379–4394.
[67] R.C. Dykhuizen, M.F. Smith, D.L. Gilmore, R.A. Neiser, X. Jiang, S. Sampath, Impact of high velocity cold spray particles, J. Therm. Spray. Technol. 8 (4) (1999) 559–564.
[68] T. Liu, J.D. Leazer, L.N. Brewer, Particle deformation and microstructure evolution during cold spray of individual Al-Cu alloy powder particles, Acta Mater. 168 (2019) 13–23.